ACS APPLIED MATERIALS & INTERFACES

Research Article

www.acsami.org

Morphology-Directing Synthesis of Rhodamine-Based Fluorophore Microstructures and Application toward Extra- and Intracellular Detection of Hg^{2+}

Rahul Bhowmick,[†] Rabiul Alam,[†] Tarun Mistri,[†] Debalina Bhattacharya,[‡] Parimal Karmakar,[‡] and Mahammad Ali*,[†]

[†]Department of Chemistry and [‡]Department of Life Science and Biotechnology, Jadavpur University, 188 Raja Subodh Chandra Mullick Road, Kolkata, West Bengal 700032, India

Supporting Information

ABSTRACT: A new, easily synthesizable rhodamine-based chemosensor with potential N_2O_2 donor atoms, $\mathbf{L^3}$, has been characterized by single-crystal X-ray diffraction together with ^1H NMR and high-resolution mass spectrometry (HRMS) studies. $\mathbf{L^3}$ was found to bind selectively and reversibly to the highly toxic Hg^{2+} ion. The binding stoichiometry and formation constant of the sensor toward Hg^{2+} were determined by various techniques, including UV−vis, fluorescence, and Job's studies, and substantiated by HRMS methods. None of the biologically relevant and toxic heavy metal ions interfered with the detection of Hg^{2+} ion. The limit of detection of Hg^{2+}calculated by the 3σ method was 1.62 nM. The biocompatibility of $\mathbf{L^3}$ with respect to its good solubility in mixed organic/aqueous media ($MeCN/H_2O$) and cell permeability with no or negligible cytotoxicity provides good opportunities for in vitro/in vivo cell imaging studies. As the probe is poorly soluble in pure water, an attempt was made to frame nano/microstructures in the absence and in the presence of sodium dodecyl sulfate (SDS) as a soft template, which was found to be very useful in synthesizing morphologically interesting $\mathbf{L^3}$ microcrystals. In pure water, micro-organization of $\mathbf{L^3}$ indeed occurred with block-shaped morphology very similar to that in the presence of SDS as a template. However, when we added Hg^{2+} to the solution of $\mathbf{L^3}$ under the above two conditions, the morphologies of the microstructures were slightly different; in the first case, a flowerlike structure was observed, and in second case, a simple well-defined spherical microstructure was obtained. Optical microscopy revealed a dotlike microstructure for $\mathbf{L^3}$−SDS assemblies, which changed to a panicle microstructure in the presence of Hg^{2+}. UV−vis absorption and steady-state and time-resolved fluorescence studies were also carried out in the absence and presence of Hg^{2+}, and also the SDS concentration was varied at fixed concentrations of the receptor and guest. The results revealed that the fluorescence intensity increased steadily with [SDS] until it became saturated at ∼7 mM SDS, indicating that the extent of perturbation to the emissive species increases with the increase in [SDS] until it becomes thermodynamically stable. There was also an increase in anisotropy with increasing SDS concentration, which clearly manifests the restriction of movement of the probe in the presence of SDS.

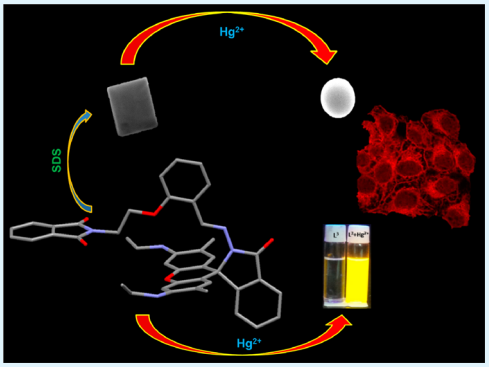

KEYWORDS: *rhodamine-based fluorophore, turn-on dual sensor, SDS-templated microstructures, cell imaging studies, optical microscopy and SEM studies*

INTRODUCTION

In recent years considerable research interest in the nano/microstructures derived from small organic molecules has grown because of their potential applications in numerous fields, including field-effect transistors, color-tunable displays, and chemical optical waveguides and sensors.[1−3] The properties of such organic nano/microstructures have been found to be intimately related to their morphologies. As a result, the fabrication of such materials is gaining intense research interest from chemists, biologists, and physicists.[4−8] Attempts have been devoted to the synthesis of organic nano/microstructured particles with various sizes and shapes, such as zero-dimensional spherical or tetrahedral quantum dots,[9] one-dimensional nanorods and wires,[10] and two-dimensional nanoplates,[11] nanoribbons and nanotubes,[8] microcapsules,[12] organic nanotowers,[13] submicrotubes,[14] etc. Although a number of synthetic strategies for preparing organic nano/microstructures, including reprecipitation,[10,15,16] solvent evaporation,[17] physical vapor deposition (PVD),[18] template-directed methods,[19,20] etc., have been developed in recent years, it is still a big challenge to develop a simple and easily-tuned route for the fabrication of organic hierarchical architectures because of the uncontrollability of intermolecular interactions and the complexities of self-assembly processes.[8,21] Out of these, reprecipitation is an

Received: July 24, 2014
Accepted: March 24, 2015
Published: March 24, 2015

DOI: 10.1021/acsami.5b01554
ACS Appl. Mater. Interfaces 2015, 7, 7476−7485

easy and versatile route that has been found to be cost-effective for the large-scale production of nano/micro building blocks.[22,23] This facile method involves solvent displacement by pouring a micromolar solution of an organic compound into a solvent where it is poorly soluble, which causes a sudden change of environment that induces the self-assembly of the organic molecules. It is widely accepted that surfactant[19,24] and polymer micelles[10,25] can be employed as an additive or template for the preparation of organic nano/microstructures.[17] Unfortunately, the size-dependent properties of organic crystals have been poorly investigated compared with those of inorganic crystals. Again, nano/microstructured materials have a close resemblance to biomaterials, offering enormous promise toward the repair of lost tissue function.[26] These also significantly influence the cell behaviors, such as morphology, adhesion, migration, proliferation, and in vitro and in vivo differentiation. As a result, research on nano/microstructured materials is gaining more and more attention in order to improve their performance and has met certain success.[27]

Because of the advantages of quick response, high sensitivity, and good selectivity, tremendous research efforts have recently been devoted to the field of chemosensing, and obviously, it has found wide applications in the fields of life sciences, environmental sciences, medical diagnostics, and toxicological analyses.[28−34] Because of the very high environmental impacts of heavy metal ions such as Hg^{2+}, Pb^{2+}, and Cd^{2+},[35] it is urgent to develop a highly selective and sensitive prove for these metal ions. Despite the fact that mercury is one of the most toxic heavy metals, it has significant applications in agriculture and industry. It is also widespread in air, water, and soil as a result of oceanic and volcanic eruptions, combustion of fossil fuels, gold mining, and solid waste incineration. Hg^{2+}, which has a high affinity for thiol groups in proteins and enzymes, causes serious health problems. Its accumulation in the body causes diseases such as prenatal brain damage, serious cognitive and motion disorders, and Minamata disease.[36] Because of these deleterious effects in humans, a highly sensitive and selective and at the same time cost-effective, rapid, and facile method is needed that would be applicable in environmental and biological milieux.[37] The most common analytical methods used for the detection and quantification of mercury include atomic absorption and emission spectroscopy,[38] inductively coupled plasma mass spectroscopy (ICP-MS),[39] inductively coupled plasma atomic emission spectrometry (ICP-AES),[40] and voltammetry.[41] However, most of these methods are either very costly or time-consuming and not suitable for performing assays. Thus, over the past decade increasing attention has been focused on the development of efficient chromo- and fluorogenic sensors for Hg^{2+} ions for real-time monitoring of environmental, biological, and industrial samples.[37,42,43] Because of its high atomic mass (A) and large spin−orbit coupling (ζ),[44] Hg^{2+} in general acts as a fluorescence quencher. However, turn-on fluorescence is always preferred over the turn-off response, as the latter may produce a false positive response due to other quencher(s) present in a practical sample.[45] As a result of its special structural features, rhodamine-based conjugates seem to be a good choice for the construction of OFF/ON fluorescent chemosensors.[46]The good photostability, high molar extinction coefficient (ε, $dm^3\ mol^{-1}\ cm^{-1}$), and a longer emission wavelength (550 nm) are added advantages to avoid background fluorescence (below 500 nm).[46−51] There are recent reports on the optical detection of Hg^{2+} in the presence and absence of gold nanoparticles.[52−56] In the present work, a new, easily synthesizable rhodamine-based probe with potential N_2O_2 donor atoms, $\mathbf{L^3}$, was synthesized and successfully employed for the selective and rapid recognition of toxic Hg^{2+}ions (Scheme 1). It exhibits chromo- and fluorogenic

Scheme 1

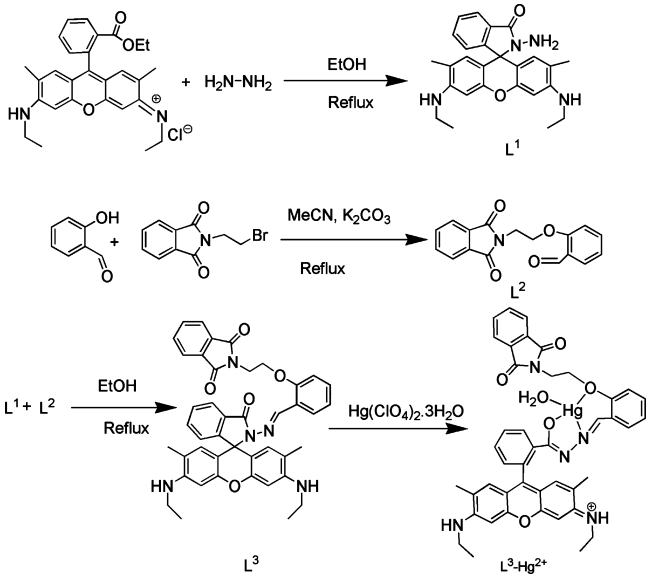

OFF/ON responses through metal-induced opening of the spirolactam ring.[57,58] The incorporation of a phthalimide moiety into the probe fragment was mainly due to its involvement in many anti-inflammatory, immunomodulatory, antiangiogenic, and antitumor drugs. Furthermore, the phthalimide moiety was screened for human liver and breast cancer cells, showing good response with minimum cytotoxicity. Hence, phthalimide is thought to be useful as a template in the development of probes suitable for in vitro/in vivo monitoring of Hg^{2+} ions with no or negligible cytoxicity.[59]

As the probe is poorly soluble in water, an attempt was made to frame nano/microstructures in the absence and in the presence of sodium dodecyl sulfate (SDS) as a template. The microstructures thereby formed were analyzed by optical microscopy and scanning electron microscopy (SEM). Not only that, we also carried out fluorescence titrations in the absence and the presence of SDS, and also, the SDS concentration was varied at fixed concentrations of the receptor and guest. The results showed a gradual increase in fluorescence intensity (FI) with the increase in SDS concentration, thereby supporting the microstructure formation. This is further strengthened by the determination of anisotropy (r) at variable concentration of SDS, which showed an increase in r with SDS concentration due to the restriction of the dynamic movement of the probe upon aggregation with SDS.

EXPERIMENTAL SECTION

Materials and Instruments. Steady-state fluorescence studies were carried out with a PTI QM-40 spectrofluorimeter. UV−vis absorption spectra were recorded with an Agilent 8453 diode array spectrophotometer. NMR spectra were recorded on a Bruker spectrometer at 300 MHz. Electrospray ionization mass spectrometry in positive-ion mode (ESI-MS^+) was performed on a Waters XEVO G2QToF (Micro YA263) mass spectrometer.

DOI: 10.1021/acsami.5b01554
ACS Appl. Mater. Interfaces 2015, 7, 7476−7485

All solvents used for synthetic purposes were of reagent grade (Merck), unless otherwise mentioned. For spectroscopic (UV−vis and fluorescence) studies, HPLC-grade MeCN and double-distilled water were used.

Rhodamine 6G hydrochloride, *N*-(2-bromoethyl)phthalimide, and metal salts such as perchlorates of Na^+, K^+, Ca^{2+}, Fe^{2+}, Co^{2+}, Ni^{2+}, Zn^{2+}, Pb^{2+}, Cd^{2+}, Hg^{2+}, and Cu^{2+} were purchased from Sigma-Aldrich and used as received. Sodium salts of anions such as SO_4^{2-}, NO_3^-, PO_4^{3-}, S^{2-}, Cl^-, F^-, Br^-, I^-, OAc^-, $H_2AsO_4^-$, and N_3^- were of reagent grade and used as received.

Preparation of Rhodamine 6G Hydrazide (L^1). Rhodamine-6G hydrazide was prepared according to a literature method.[60]

Preparation of 2-[2-(1,3-Dioxo-1,3-dihydroisoindol-2-yl)-ethoxy]benzaldehyde (L^2). In a typical procedure, salicylaldehyde (10 mmol, 1.23 g) was dissolved in dry MeCN (60 mL), to which K_2CO_3 (18 mmol, 2.52 g) was added, and the mixture was heated at reflux for 40 min. *N*-(2-Bromomethyl)phthalimide (10 mmol, 2.54 g) and a catalytic amount of KI (0.15 g) were then added to the above reaction mixture, and reflux was continued for another 15 h. The mixture was then cooled to room temperature and filtered. The filtrate was evaporated to one-third of its initial volume and diluted with 40 mL of water. The pH of the resulting solution was then adjusted to 4 by the addition of 1 M HCl, and the mixture was extracted with dichloromethane (DCM) (2 × 40 mL). The pH of the aqueous solution was further adjusted to 8 by the addition of 4.0 M Na_2CO_3 solution, and the solution was extracted with DCM (3 × 40 mL). The combined organic phases were dried over anhydrous Na_2SO_4 and then evaporated to dryness under reduced pressure to afford a reddish-yellow solid. The solid product was recrystallized from MeCN/DCM (8:2 v/v) to give the desired NMR-pure product as a crystalline solid in 84% yield. ^{1}H NMR ($CDCl_3$): δ = 10.24 (s, 1H), 7.84 (m, 4H), 7.59 (m, 2H), 7.17 (d, 1H, J = 7.9 Hz), 7.02 (d, 1H, J = 7.4 Hz), 4.31 (t, 2H, J = 5.0 Hz), 4.05 (t, 2H, J = 5.0 Hz) ppm (Figure S1). MS (ES^+): m/z = 296.1353 $[L + H]^+$ (Figure S2).

Preparation of Probe L^3. L^2 (1.10 mmol, 0.324 g) in MeOH (10 mL) was added dropwise to a methanolic solution (30 mL) of L^1 (1 mmol, 0.428 g) containing 1 drop of acetic acid under hot (50−60 °C) conditions over 30 min, and the mixture was then stirred for about 6 h at room temperature, whereupon the yellow precipitate formed was collected by filtration. The residue was washed thoroughly with cold methanol to isolate L^3 in pure form in 78% yield. Single crystals of L^3 were obtained by recrystallization from DCM/MeCN (1:1 v/v). ^{1}H NMR (DMSO-d_6): δ = 8.49 (s, 1H), 7.91 (m, 5H), 7.55 (m, 3H), 7.26 (t, 1H, J = 6.4 Hz), 6.92 (m, 3H), 6.32 (s, 2H), 6.14 (s, 2H), 5.04 (s, 2H), 3.97 (m, 4H), 3.11 (m, 4H), 1.82 (s, 6H), 1.17 (t, 6H, J = 7.0 Hz) ppm (Figure S3). IR: $\tilde{\nu}$ = 1713.95 cm^{-1} (spirolactam amide keto), 1620.91 cm^{-1} (−C═N) (Figure S4). MS (ES^+): m/z = 706.3329 $[L + H^+]$ (Figure S5).

Preparation of the L^3−Hg^{2+} Complex. $Hg(ClO_4)_2$ (0.272 g, 0.6 mmol) was added to a 10 mL MeCN solution of L^3 (0.350 g, 0.5 mmol), and the mixture was stirred for about 30 min. It was then filtered and allowed to evaporate slowly at ambient temperature to get the crystalline solid product. ^{1}H NMR (DMSO-d_6): δ = 8.90 (s, 1H), 7.88 (m, 5H), 7.57 (m, 3H), 7.26 (s, 1H), 6.93 (m, 3H), 6.34 (s, 2H), 6.15 (s, 2H), 5.72 (s, 1H), 3.97 (m, 4H), 3.11 (m, 4H), 1.82 (s, 6H), 1.17 (t, 6H, J = 7.0 Hz) ppm (Figure S6). IR: $\tilde{\nu}$ = 1653.81 cm^{-1} (spirolactam ring open), 1608.05 cm^{-1} (−C═N) (Figure S4). MS (ES^+): m/z = 1078.4314 $[(L^3)Hg(CH_3OH)(H_2O)(ClO_4)]Na^+$ (Figure S7).

Solution Preparation for UV−Vis and Fluorescence Studies. For both UV−vis and fluorescence titrations, a 1.0 × 10^{-3} M stock solution of L^3 was prepared by dissolving the ligand in 7 mL of MeCN and then increasing the volume to 10 mL with deionized water. Similarly, a 1.0 × 10^{-3} M stock solution of Hg^{2+} was prepared in deionized H_2O. A 250 mL 5 mM HEPES buffer solution was prepared, and the pH was adjusted to 7.2 using HCl and NaOH. Then 2.5 mL of this buffer solution was pipetted into a cuvette, to which the required volume of 1.0 × 10^{-3} M probe solution was added to get a final concentration of 20 μM for UV−vis titrations and 5 μM for fluorescence titrations. Hg^{2+} ion solution was added incrementally in regular intervals of volume, and UV−vis or fluorescence spectra were recorded for each solution. The path lengths of the cells used for absorption and emission studies were 1 cm. Fluorescence measurements were performed using a 2 nm × 2 nm slit.

For competition assays, a 1.0 × 10^{-3} M Na_2H_2EDTA solution was prepared in water. Then 2.5 mL of the buffer solution was pipetted into a cuvette, to which the L^3 and Hg^{2+} solutions (10 μM each) were added. Na_2H_2EDTA solution was added to this solution incrementally to a final volume of 14 μM in a regular interval of volume, and fluorescence spectra were recorded for each solution upon excitation at 510 nm. The equilibria related to the competition assays are the following:

$$M + L_1 \overset{K_{L_1}}{\rightleftarrows} M{-}L_1$$

$$M + L_2 \overset{K_{L_2}}{\rightleftarrows} M{-}L_2$$

$$M{-}L_1 + L_2 \overset{K_{comp}}{\rightleftarrows} M{-}L_2 + L_1$$

$$K_{comp} = \frac{[M{-}L_2][L_1]}{[M{-}L_1][L_2]} = \frac{K_{L_2}}{K_{L_1}}$$

where M = Hg^{2+}, L_1 = L^3, L_2 = H_2EDTA^{2-}, M−L_1 = Hg^{2+}−L^3, and M−L_2 = $[Hg^{2+}$−EDTA$]^{2-}$. The competition equilibrium constant (K_{comp}) was calculated from the titration curve:

$$[M{-}L_2] = \frac{[M]_T + [L_2]_T K_{comp} + [M]_T K_{comp}}{[2(-1 + K_{comp})]} - \{-4[L_2]_T[M]_T(-1 + K_{comp})K_{comp} + ([M]_T - [L_2]_T K_{comp} - [M]_T K_{comp} - [L_1])^2 + [L_1]\}^{1/2} / [2(-1 + K_{comp})]$$

where $[M]_T$ is the total concentration of Hg^{2+}, $[L_1]_T$ is the concentration of L^3, and $[L_2]_T$ is the total concentration of H_2EDTA^{2-}, and $[M{-}L_2]$ is the concentration of the complex between H_2EDTA^{2-} and Hg^{2+}. The fitting of the titration profiles with a non linear least-squares procedure using the competition model provides the value of K_{comp}.[61]

Preparation of L^3 Microbar Samples. We prepared 10 mL each of 1 mM, 10 mM, and 100 mM stock solutions of the ligand and 10 mL of 1 mM stock solution of SDS. Then 1 mL of each ligand solution was added to 1 mL of SDS solution with stirring for 5 min. The concentrations of SDS/L^3 in the resulting solutions were (a) 0.50/0.50 mM, (b) 0.55/5.0 mM, and (c) 0.50/50 mM, respectively. The use of higher concentrations of SDS (up to 7.5 mM) did not show any major change in the formation of the microstructures. For the variation of the SDS concentration, we prepared a 200 mM stock solution of SDS from which we added SDS to 2.5 mL solutions of L^3 (5 μM) and Hg^{2+} (5 μM) to give overall SDS concentrations of 0.5, 1.0, 1.5, 2.0, 2.5, 3.0, 3.5. 4.0, 4.5, 5.0, 5.5, 6.0, 6.5, and 7.0 mM in the 2.5 mL reaction solutions. In another set of solutions, equivalent amounts of Hg^{2+} with respect to ligand concentration were added. After 5 min of stirring, the solutions were aged overnight at room temperature before characterization. The samples in both cases were found to give the best microstructure and analyzed by optical microscopy and SEM.

Methods of Characterization. An upright optical microscope (Olympus polarized optical microscope, model BX51) was used to study the morphology of the materials both in the absence and in the presence of variable concentrations of SDS, and images were taken using a 12 V, 50 W mercury lamp. Optical microscopy studies were performed on the samples prepared by placing a drop of solution onto a clean glass slide. A JEOL JSM 8360 scanning electron microscope operated at an accelerating voltage of 5 kV was used for the study of morphologies of the above samples. Before SEM analysis, the samples

DOI: 10.1021/acsami.5b01554
ACS Appl. Mater. Interfaces 2015, 7, 7476−7485

were vacuum-dried, and a thin layer of Au was deposited onto the samples to minimize sample charging.

Steady-state fluorescence and fluorescence anisotropy measurements were done on a PTI QM-40 spectrofluorometer. The fluorescence anisotropy (r) is defined as

$$r = \frac{I_{VV} - GI_{VH}}{I_{VV} + 2GI_{VH}} \quad (1)$$

where I_{VV} and I_{VH} are the emission intensities obtained with the excitation polarizer oriented vertically and the emission polarizer oriented vertically and horizontally, respectively, and the corresponding G factor is calculated as[46]

$$G = I_{HV}/I_{HH} \quad (2)$$

where the intensities I_{HV} and I_{HH} refer to the vertical and horizontal positions of the emission polarizer with the excitation polarizer being horizontal.

Cell Culture. The HeLa cell lines of human cervical cancer origin were purchased from the National Center for Cell Science (Pune, India) and cultured using the protocol described elsewhere.[62−64]

Cell Imaging Studies. Cell imaging studies were performed using the protocol described previously.[62−64] A 1.0 mM stock solution of $\mathbf{L}^3$ was prepared by dissolving it in a mixed solvent (DMSO/water = 1:9 v/v). HeLa cells were rinsed with phosphate-buffered saline (PBS) and incubated for 30 min at room temperature with Dulbecco's modified Eagle's medium (DMEM) containing $\mathbf{L}^3$, making the final concentration up to 10 μM in DMEM. Then bright-field and fluorescence images of the cells were taken with a confocal fluorescence microscope. Similarly, fluorescence images were taken separately for the HeLa cells incubated for 30 min with (i) 10 μM $\mathbf{L}^3$ + 10 μM Hg^{2+} and (ii) 10 μM $\mathbf{L}^3$ + 10 μM Hg^{2+} + 100 μM KI.

We also ran parallel experiments to study the effect of thiol (i.e., cysteine) on the $\mathbf{L}^3$−Hg^{2+} complex. For this purpose, after incubation cells were washed twice with 1× PBS and counterstained with 4′,6-diamidino-2-phenylindole dihydrochloride (DAPI), used for nuclear staining (Sigma). Fluorescence images of the cells were taken using a fluorescence microscope (Leica DM3000, Germany) with an objective lens of 40× magnification. Fluorescence images of HeLa cells were taken separately from another set of experiments where the cells were preincubated with 10 μM Hg^{2+} for 30 min at 37 °C, washed twice with 1× PBS, and subsequently incubated with 10 μM $\mathbf{L}^3$ for 30 min at 37 °C. Similarly, in another set of experiments, cells were incubated sequentially with 10 μm Hg^{2+}, 10 μM $\mathbf{L}^3$, and 10, 20, and 50 μM cysteine for 30 min at 37 °C with alternative washing with 1× PBS two times.

Cell Cytotoxicity Assay. To test the cytotoxicity of $\mathbf{L}^3$, the 3-(4,5-dimethylthiazol-2-yl)-2,5-diphenyltetrazolium bromide (MTT) assay was performed following the procedure described previously.[62−64] The cell viability was expressed as the ratio of the optical densities of the treated sample and control. Values are expressed as means of three independent experiments. The cell cytotoxicity is given by 100% − (% cell viability).

RESULTS AND DISCUSSION

A Schiff base condensation between $\mathbf{L}^1$ and $\mathbf{L}^2$ in methanol (Scheme 1) afforded the sensor $\mathbf{L}^3$, which was thoroughly characterized by ^{1}H NMR and IR spectroscopy and ESI-MS$^+$. The structure of the probe was also analyzed by single-crystal X-ray diffraction studies (see Table T1 in the Supporting Information), and the ORTEP view is shown in Figure 1.

Optical Microscopy Studies. Under the optical microscope, it was observed that the formation of well-defined branched panicle geometry takes place under conditions (a) in the presence of Hg^{2+}. In the absence of metal ions, the microstructures are like microdots (Figure 2A and Figure S9A). A dark-field view of the sample using a polarizer and analyzer

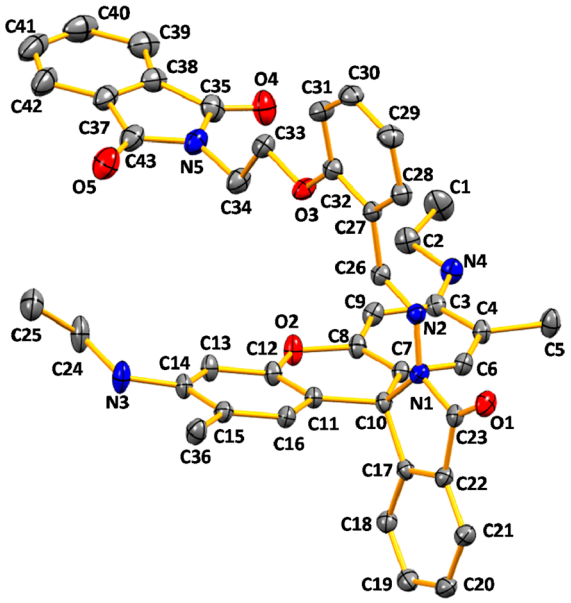

Figure 1. ORTEP view (30% ellipsoid probability) of ligand $\mathbf{L}^3$ (all H atoms have been omitted for clarity).

assembly shows the luminescence property of the assemblies (Figure 2B and Figure S9B).

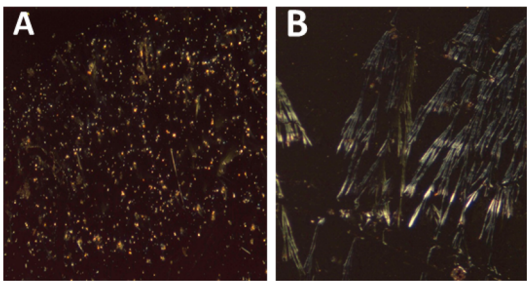

Figure 2. Polarized optical microscopy images of (A) $\mathbf{L}^3$−SDS microcrystals (microdots) having 0.5 mM each and (B) $\mathbf{L}^3$−SDS−Hg^{2+} microcrystals (micropanicles) having 0.5 mM each.

SEM Studies. As the probe is poorly soluble in pure water, an attempt was made to frame nano/microstructures in the absence and presence of SDS as a soft template, which was found to be very useful in synthesizing morphologically interesting $\mathbf{L}^3$ microcrystals. In pure water, macro-organization of $\mathbf{L}^3$ indeed occurred, giving a block-shaped morphology very similar to that formed in the presence of SDS as a template. However, when we added Hg^{2+} to the solution of $\mathbf{L}^3$ under the above two conditions, the morphologies of the microstructures were slightly different; in the first case, a flowerlike structure was observed, and in the second case, simply a well-defined spherical microstructure was obtained.

For SEM studies we prepared samples with (Figure 3) and without SDS (Figure S10) both in absence and in the presence of Hg^{2+}. A distinct change in morphology from block to spherical shape was observed upon addition of metal ion to the solution containing SDS and $\mathbf{L}^3$ (0.5 mM each). The most interesting feature of this study is that in both cases (in absence and presence of SDS), the block-shaped microstructures changed to spherical ones in the presence of Hg^{2+} ions. One explanation may be furnished by the fact that the coordination of the free ligands along the edges of the block are not satisfied

DOI: 10.1021/acsami.5b01554
ACS Appl. Mater. Interfaces 2015, 7, 7476−7485

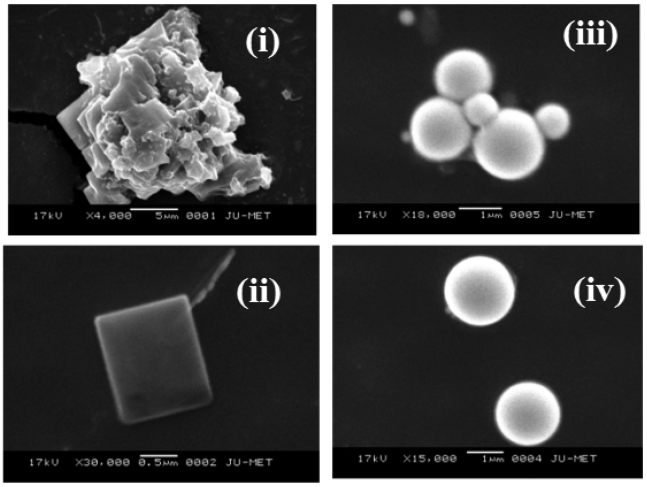

Figure 3. SEM images of microstructures. Conditions: (i, ii) L^3–SDS (0.5 mM each) in (i) 5 μM (4000×) and (ii) 0.5 μM (30000×); (iii, iv) L^3–SDS–Hg^{2+} (0.5 mM each) in (iii) 1 μM (10000×) and (iv) 1 μM (15000×).

and are highly reactive; they easily bind to Hg^{2+} ions and come out of the edges, thereby transforming the block microstructure to a spherical one.

Steady-State Absorption and Emission Studies. The UV–vis titrations were carried out in the presence as well as in the absence of SDS with a fixed concentration of L^3 (20 μM) and variable concentration of Hg^{2+} (0–25.0 μM) at 25 °C in aqueous MeCN (3:7 v/v, HEPES buffer, pH 7.2). It was observed that under both sets of conditions there is a gradual development of a new absorption band at around 529 nm upon addition of Hg^{2+} (Figure 4A), and it becomes saturated upon

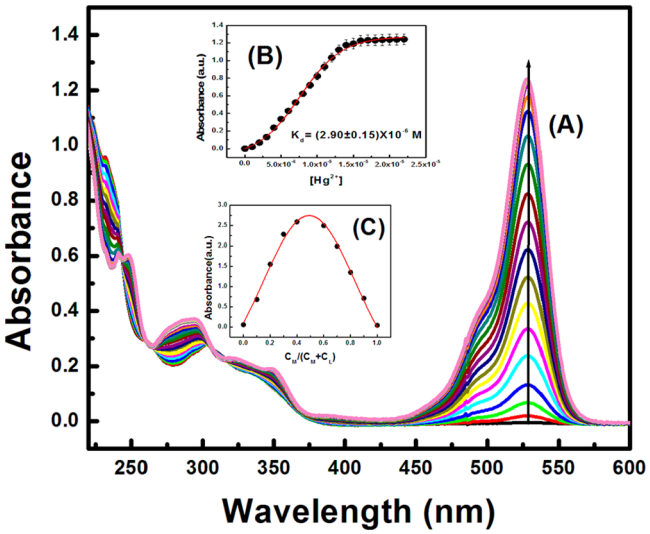

Figure 4. (A) Absorption titration of L^3 (20.0 μM) with Hg^{2+} in MeCN/H_2O (7:3 v/v) in HEPES buffer (1 mM) at pH 7.2; (B) nonlinear fitting of the data; (C) Job's plot.

addition of ≥1.0 equiv of Hg^{2+} (Figure 4B), the concentration of L^3 being fixed at 20.0 μM. The binding constant of the formed L^3–Hg^{2+} complex was determined by utilizing a suitable nonlinear fitting computer program, which gave K_d = (2.90 ± 0.15) × 10^{-6} M.

Job's method was employed to determine the composition of the complex, which was found to be 1:1 (Figure 4C). This was further supported by mass spectrometric analysis (m/z = 1078.4314 $[Hg(L^3)(MeOH)(H_2O)(ClO_4)]Na^+$; see Figure S7).

The emission spectra of L^3 and its fluorescence titration with Hg^{2+} were performed in MeCN/water solution (7:3 v/v, HEPES buffer, pH 7.2) with a fixed concentration of L^3 (5 μM) Figure 5A). Upon gradual addition of Hg^{2+} (0–5.0 μM) to the

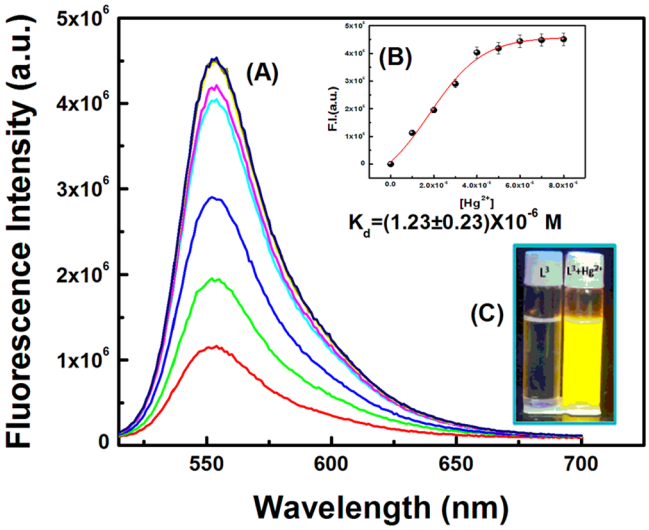

Figure 5. (A) Fluorescence titration of L^3 (5.0 μM) in MeCN/H_2O (7:3 v/v) in HEPES buffer at pH 7.2 by the gradual addition of Hg^{2+} with λ_{ex} = 510 nm and λ_{em} = 552 nm. (B) Nonlinear curve fitting of the FI vs $[Hg^{2+}]$ plot. (C) UV-exposed images of L^3 and L^3 + Hg^{2+}.

nonfluorescent solution of L^3 (5.0 μM), a 52-fold enhancement in fluorescence intensity at 552 nm was observed following excitation at 510 nm, which also suggests the opening of the spirolactam ring in L^3 upon coordination to the Hg^{2+} ion.[58] The nonlinear least-squares fit of the fluorescence titration data of L^3 with Hg^{2+} gave an apparent association constant K_f' of (1.23 ± 0.23) × 10^{-6} M^{-1} (see Figure 5B) directly. We also attempted to determine the apparent formation constants by the competition method by reacting the in situ-generated complexes like $[Hg^{2+}–L^3]$ with Na_2H_2EDTA, and equilibrium competition constants (K_{f1}') were calculated from the plots of FI as a function of H_2EDTA^{2-} concentration by adopting a displacement model (see Figure S11). The evaluated apparent formation constant is K_{f1}' = (1.64 ± 0.17) × 10^5 M^{-1}, and corresponding formation constant K_f was calculated from the relation $K_f = K_f'/K_{EDTA}'$ (where $K_{EDTA}' = \alpha_4 K_{EDTA}$ = 8.19 × 10^{18}, where $\alpha_4 = K_1K_2K_3K_4/([H^+]^4 + K_1[H^+]^3 + K_1K_2[H^+]^2 + K_1K_2K_3[H^+] + K_1K_2K_3K_4)$ = 1.30 × 10^{-3} at pH 7.20, K_1 = 1.02 × 10^{-2}, K_2 = 2.14 × 10^{-3}, K_3 = 6.92 × 10^{-7}, K_4 = 5.50 × 10^{-11}, and $K_{Hg\text{-}EDTA}$ = 6.30 × 10^{21}).[65] So the calculated value is K_f' = 4.83 × 10^5. The apparent formation constant obtained directly from the fluorescence titration, K_f' = (1.30 ± 0.17) × 10^5 M^{-1}, is very close to the value obtained by the competition method.

There is a reasonable agreement between the values of K_d extracted from the absorption and fluorescence titrations, manifesting the self-consistency of our results. Upon exposure of the solution to UV radiation, there is a detectable change in the color from colorless to orange-yellow (Figure 5C), which

DOI: 10.1021/acsami.5b01554
ACS Appl. Mater. Interfaces 2015, 7, 7476–7485

clearly demonstrates the formation of the ring-opened amide form of L^3 upon binding to Hg^{2+}.[58]

The detection of Hg^{2+} was not perturbed by the presence of biologically abundant metal ions such as Na^+, K^+, Ca^{2+}, and Mg^{2+}. Likewise, under identical reaction conditions no significant color or spectral change was observed for transition-metal ions, namely, Cr^{3+}, Mn^{2+}, Fe^{2+}, Fe^{3+}, Co^{2+}, Cu^{2+}, Ni^{2+}, and Zn^{2+}, and heavy-metal ions, including $Cd^{2+}$and Pb^{2+} (Figure S12). The pH stability of the probe was checked over a wide range of pH (2−12), and it was interesting to note that there was no obvious fluorescence emission of L^3 between pH 4 and 12, suggesting a convenient application of this probe under physiological conditions and also establishing the fact that the spirolactam form of L^3 is stable over this wide range of pH (Figure 6). However, in the presence of a selective guest

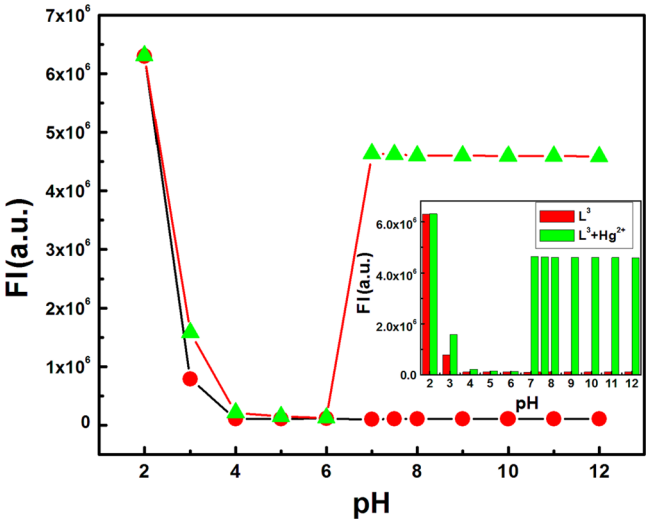

Figure 6. pH dependence of the FIs of the free ligand L^3 (red) and the L^3−Hg^{2+} complex with L^3:Hg^{2+}= 1:1.05 (green) in the MeCN/H_2O (7:3 v/v) solvent system with λ_{ex} = 510 nm. The inset shows the histogram plot.

such as Hg^{2+} ion it fluoresces effectively at pH ≥ 7.0, indicating the compatibility of the probe for biological applications under physiological conditions.

In addition to the above studies in MeCN/water (7:3 v/v, HEPES buffer, pH 7.2) at a fixed concentration of L^3 (5 μM), we also carried out this titration in pure water in the presence of SDS under two conditions: (i) at fixed concentrations of L^3 (5 μM) and SDS (0.5 mM) and variable concentration of Hg^{2+} and (ii) at fixed concentrations of L^3 and Hg^{2+} (5 μM each) and variable concentration of SDS from 0 to 7.0 mM. Under the first set of conditions, there was also an increase in FI with increasing Hg^{2+} concentration (Figure S13) until the FI reached a maximum at ∼5.0 mM Hg^{2+}, after which it remained almost constant upon further increases in the Hg^{2+} concentration. A nonlinear least-squares method was adopted to get the K_d value of (7.48 ± 0.93) × 10^{-7} M^{-1}, which is slightly lower than that obtained in MeCN/H_2O in the absence of SDS. This indicates higher stability of the formed complex in the presence of SDS. Under the second set of conditions, a gradual increase in FI was observed with increasing SDS concentration (Figure 7). A plot of FI vs [SDS] gave a nonlinear curve with decreasing slope. This experiment clearly demonstrates aggregation between L^3−Hg^{2+} and SDS that is favored with increasing SDS concentration.

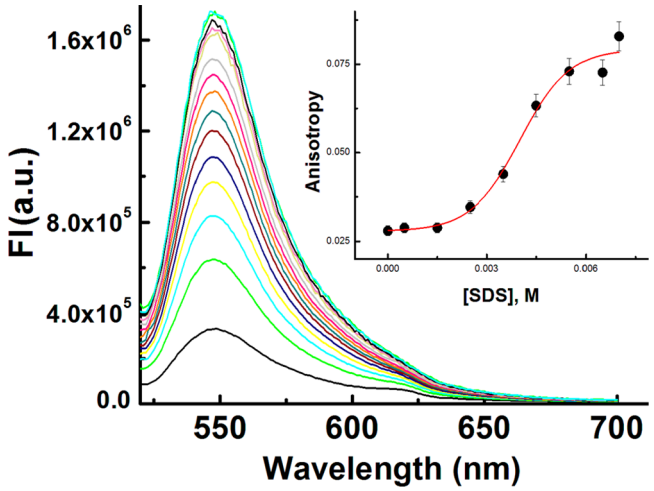

Figure 7. Plot of fluorescence intensity as a function of SDS concentration. The inset shows the plot of the fluorescence anisotropy (r) as a function of SDS concentration.

Steady-State Fluorescence Anisotropy. Steady-state fluorescence anisotropy is used to monitor the extent of restriction imposed on the dynamic properties of the probe by the microenvironment and is widely exploited to assess the motional information in such heterogeneous microenvironments.[46,66] An increase in rigidity of the fluorophore results in an increase in the fluorescence anisotropy. The fluorescence anisotropy was monitored as a function of SDS concentration at fixed concentrations of L^3 and Hg^{2+} (5 μM each) at 553 nm. The fluorescence anisotropy monitoring of this band showed a marked increase in anisotropy with increasing SDS concentration, which indicates that the fluorophore moved from the aqueous phase to the SDS environment, causing the rotational diffusion of the probe molecule to be restricted significantly. The variation of the fluorescence anisotropy (r) as a function of SDS concentration is presented in the inset of Figure 7.

Selectivity of the Probe. The reversible binding of L^3 to Hg^{2+} was investigated under reaction conditions identical to those adopted in the absorption and fluorescence titrations (see Figure 8). Anions such as SO_4^{2-}, NO_3^-, PO_4^{3-}, S^{2-}, Cl^-, F^-, Br^-, I^-, OAc^-, $H_2AsO_4^-$, and N_3^- (5 equiv relative to L^3) were introduced (Figure S14) into the solution containing Hg^{2+} and

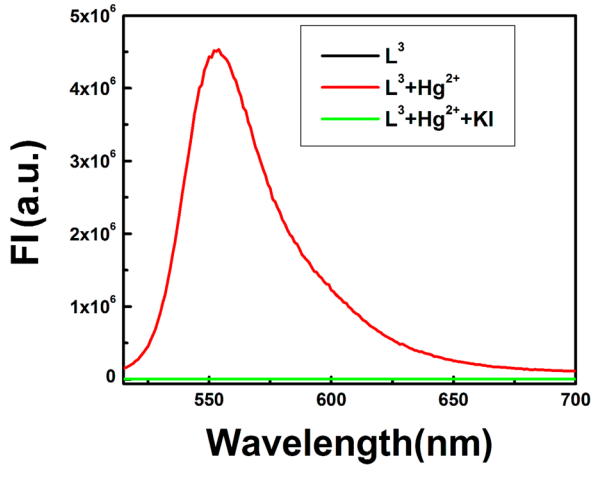

Figure 8. Test of reversible binding of L^3 toward Hg^{2+} in the presence of KI.

DOI: 10.1021/acsami.5b01554
ACS Appl. Mater. Interfaces 2015, 7, 7476−7485

ligand L^3, and subsequently, the changes in the fluorescence intensity were monitored. The results showed that I^- has a strong affinity toward Hg^{2+}, and its binding constant is expected to be much higher than that of L^3. This results in the abstraction of Hg^{2+} from the L^3–Hg^{2+} complex, leading to the disappearance of the emission band at 553 nm through the reestablishment of the spirolactam ring (Figure 8). The quantum yield of the L^3–Hg^{2+} complex was determined to be Φ = 0.65 (using rhodamine 6G as a standard). The free ligand was found to be non- or very weakly fluorescent with a very negligible absorption band at 529 nm. The 3σ method was adopted to determine the limit of detection (LOD) of Hg^{2+}, which was found to be as low as 1.62 nM (Figure S16). All of these findings indicate that L^3 behaves as a good example of an ideal chemosensor for Hg^{2+}.

IR and ^{1}H NMR studies were carried out to shed some light on the mechanistic pathway for the formation of the L^3–Hg^{2+} complex, which was found to occur by opening of the spirolactam ring. The characteristic stretching frequency of the amidic "C═O" of the rhodamine moiety at 1713.95 cm^{-1} is shifted to a lower wavenumber (1653.81 cm^{-1}) in the presence of 1.2 equiv of Hg^{2+} (Figure S4), indicating not only strong polarization of the C═O bond upon efficient binding to the Hg^{2+} ion but also in fact the cleavage of N–C bond in the spirolactum ring. Also, the ^{1}H NMR spectra show a downfield shift of the ring protons of the rhodamine moiety (e, f, and g; see the labeling in Figure 9) in the presence of 1.2 equiv of

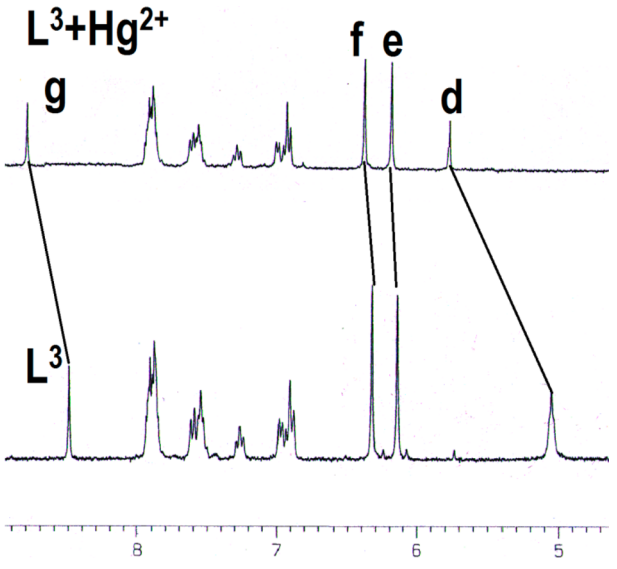

Figure 9. ^{1}H NMR shifts of L^3 and L^3 + Hg^{2+}.

Hg^{2+} ions. Proton d shows an upfield shift that is mainly due to an increase in electron density arising from the opening of the spirolactam ring. The complex signal pattern of the other aromatic protons also indicates the involvement of the pyridine moiety of the receptor unit of L^3 in the binding of Hg^{2+}.

In order to ascertain the nonparticipation of the phthalimide moiety toward binding with Hg^{2+}, we prepared two other probes, L^4 and L^5, and tested their binding with Hg^{2+} ion. It was observed that L^4 binds solely to Hg^{2+} with a comparable K_f' value (K_f' = 5.9 × 10^5 M^{-1}) while L^5 binds to both Hg^{2+} (K_f' = 5.4 × 10^5 M^{-1}) and Cd^{2+} (K_f' = 1.96 × 10^5 M^{-1}). The plots of FI versus [M^{2+}] (M = Hg, Cd) are shown in Figure S20a–c.

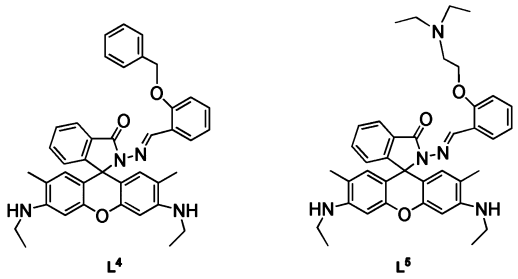

Cell Imaging Experiments. The intracellular Hg^{2+} imaging behavior of L^3 was studied in HeLa cells using fluorescence microscopy. After incubation with L^3 (10 μM), the cells displayed no intracellular fluorescence (Figure 10). However,

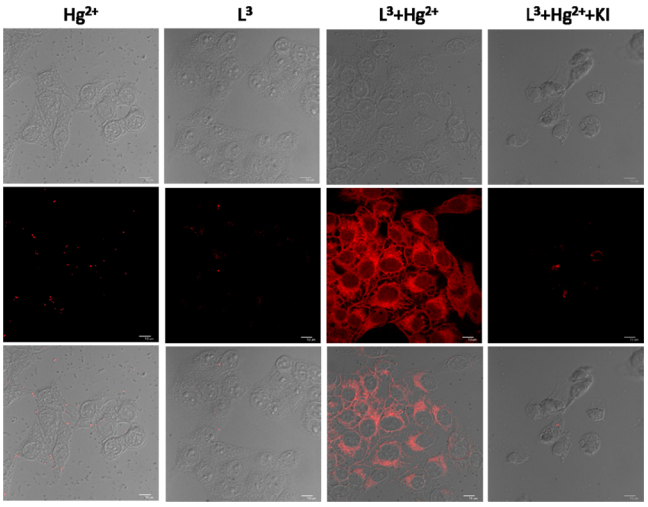

Figure 10. Phase-contrast and fluorescence images of HeLa cells in a confocal microscope captured after incubation with L^3 or L^3 + Hg^{2+} for 30 min at 37 °C and following addition of 100 μM KI after the cells were preincubated with L^3 + Hg^{2+} for 30 min at 37 °C.

the cells exhibited intense fluorescence when a solution of $Hg(ClO_4)_2$ (10 μM) was added to the L^3-preincubated cells (Figure 10). Interestingly, we observed that the fluorophore L^3 shows only cytoplasmic binding with Hg^{2+}, not nuclear binding (Figure 10). This specific binding of the fluorophore to cytoplasm safely avoids any genetic damage. Again, the fluorescence was strongly suppressed upon the addition of KI (100 μM) to this medium (Figure 10), indicating strong scavenging action on Hg^{2+} through the formation of very stable HgI_2 species. Here the fluorescence almost disappeared through the re-establishment of the spirolactam ring (Figure 10). This confirms that L^3 can monitor the change in intracellular concentration of Hg^{2+} ions under different biological conditions in a biological system, particularly because of its relatively low cytotoxicity for up to 5 h (Figure S17) and very low LOD value.

We checked the thiophilicity of Hg^{2+} ions using cysteine under both extra- and intracellular conditions. It was observed that there was negligible change (decrease) in FI upon addition of 1 equiv of the thiol (10 μM) to an ensemble of 10 μM L^3–Hg^{2+}. This clearly indicates that the probe could be used to detect Hg^{2+} intracellularly in the presence of thiols to a concentration of at least 10 μM, as best viewed in Figures S18 and S19.

DOI: 10.1021/acsami.5b01554
ACS Appl. Mater. Interfaces 2015, 7, 7476–7485

A few of the recently investigated rhodamine 6G-based Hg^{2+} sensors are shown in Scheme 2, and some of their salient

Scheme 2

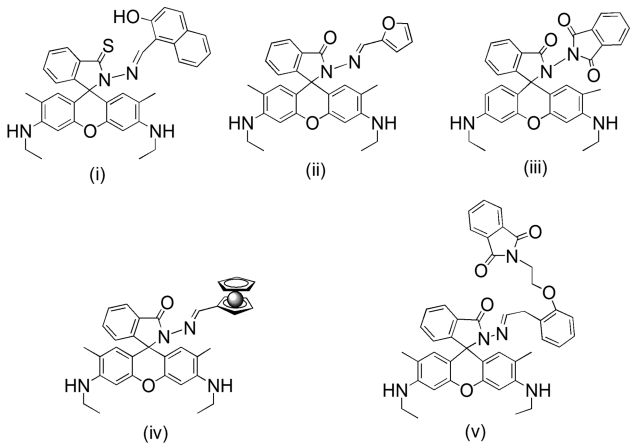

Table 1. Comparison of Results for Rhodamine 6G-Based Probes for Recognizing Hg^{2+}

probe	formation constant	LOD	cell study	microstructure
(i)	1.16×10^6 M^{-1}	ppb	done	–
(ii)	3.07×10^5 M^{-1}	0.35 ppb	done	–
(iii)	5.2×10^5 M^{-1}	–	done	–
(iv)	8.42×10^4 M^{-1}	–	done	–
(v)	3.4×10^5 M^{-1}	1.62 nM	done, cytoplasmic binding is apparent	done with distinct morphologies in the absence and presence of Hg^{2+}

features are given in Table 1. A quick inspection of the results reveals that all of these are turn-on Hg^{2+} ion sensors with moderate LOD values (~nM) and are applicable for monitoring of intracellular Hg^{2+} ion.[67−70] Both probe (iii) and our system (v) contain a phthalimide functional group and provide very similar formation constants and cell imaging behavior, although probe (iii) is not selective, as it also recognizes Cr^{3+} along with Hg^{2+}. In that sense, our probe (v) seems to be superior to (iii) because it is selective for Hg^{2+} and also forms block-shaped microstructures that change to spherical ones upon addition of Hg^{2+} in aqueous solution.

CONCLUSION

In summary, we have presented herein a new type of easily synthesizable rhodamine-based chemosensor with potential N_2O_2 donor atoms for the selective and rapid recognition of toxic Hg^{2+} ions, which has been characterized by ^1H NMR, HRMS, and IR studies. The binding stoichiometry of the sensor with Hg^{2+} was established by the combination of UV−vis, fluorescence, Job's, and HRMS methods. None of the biologically relevant metal ions or toxic heavy metals such as $Cd^{2+}$and Pb^{2+} interfered with the detection of Hg^{2+} ion. The detection limit of Hg^{2+} calculated by the 3σ method was 1.62 nM. The biocompatible nature of the probe with respect to its good solubility in mixed organic/aqueous media (MeCN/H_2O) along with its cell permeability with no or negligible cytotoxicity provides a good opportunity for in vitro/in vivo cell imaging studies. The cytoplasmic binding makes this probe more appropriate for in vivo monitoring of Hg^{2+} without any genetic damage. As the probe is poorly soluble in water, an attempt was made to frame nano/microstructures in the absence and presence of SDS as a soft template, which gave interesting block-shaped microcrystals for $\mathbf{L}^3$ under both conditions. But upon addition of Hg^{2+} to these solutions, spherical microstructures were obtained in the presence of SDS and flowerlike microstructures in the absence of it. This distinct change in morphology from block to spherical shape upon addition of metal ion to the solution of $\mathbf{L}^3$ or $\mathbf{L}^3$−SDS may be explained by considering the fact that the coordination of the free ligands along the edges of the blocks are not satisfied, and the ligands are highly reactive and easily bind to Hg^{2+} ions, causing them to come out of the edges, thereby transforming the block microstructures to spherical ones.

Under an optical microscope, a dotlike microstructure was found upon SDS−$\mathbf{L}^3$ aggregation, which was totally changed into a branched panicle microstructure in the presence of Hg^{2+}. In addition, we also carried out fluorescence titrations in the absence and presence of SDS and also by varying the SDS concentration at fixed concentrations of the receptor and the guest. The studies clearly indicate that the extent of perturbation of the emissive species continues to increase until it reaches a thermodynamically stable structure. The increase in anisotropy with increasing SDS concentration clearly demonstrates that SDS favors the formation of microstructures by imposing restrictions on their free movements.

ASSOCIATED CONTENT

Supporting Information

Information on the synthesis and corresponding characterization data for compound $\mathbf{L}^3$, preparation of test strips, absorption spectra, and ^1H NMR spectra. This material is available free of charge via the Internet at http://pubs.acs.org.

AUTHOR INFORMATION

Corresponding Author

*E-mail: m_ali2062@yahoo.com.

Notes

The authors declare no competing financial interest.

ACKNOWLEDGMENTS

Financial support from the Department of Science and Technology (DST), Government of India, New Delhi (SR/S1/IC-20/2012) is gratefully acknowledged. The use of instumental facilities (FE-SEM) from the Department of Physics (DST-FIST) is gratefully acknowledged.

REFERENCES

(1) Zhao, Y. S.; Fu, H.; Peng, A.; Ma, Y.; Xiao, D.; Yao, J. Low-Dimensional Nanomaterials Based on Small Organic Molecules: Preparation and Optoelectronic Properties. *Adv. Mater.* **2008**, *20*, 2859−2876.

(2) Tang, Q.; Jiang, L.; Tong, Y.; Li, H.; Liu, Y.; Wang, Z.; Hu, W.; Liu, Y.; Zhu, D. Micrometer- and Nanometer-Sized Organic Single-Crystalline Transistors. *Adv. Mater.* **2008**, *20*, 2947−2951.

(3) Zhao, Y. S.; Fu, H.; Peng, A.; Ma, Y.; Liao, Q.; Yao, J. Construction and Optoelectronic Properties of Organic One-Dimensional Nanostructures. *Acc. Chem. Res.* **2010**, *43*, 409−418.

DOI: 10.1021/acsami.5b01554
ACS Appl. Mater. Interfaces 2015, 7, 7476−7485

(4) Birla, L.; Bertorelle, F.; Rodrigues, F.; Badré, S.; Pansu, R.; Fery-Forgues, S. Effects of DNA on the Growth and Optical Properties of Luminescent Organic Microcrystals. *Langmuir* **2006**, *22*, 6256−6265.
(5) Zhang, T. K.; Zhu, J. H.; Yao, H. B.; Yu, S. H. Novel Fluorescein Hierarchical Structures Fabricated by Recrystallization under Control of Polyelectrolytes. *Cryst. Growth Des.* **2007**, *7*, 2419−2428.
(6) Wang, Y.; Fu, H.; Peng, A.; Zhao, Y. S.; Xiao, D.; Ma, J.; Ma, Y.; Yao, J. Distinct Nanostructures from Isomeric Molecules of Bis-(iminopyrrole)benzenes: Effects of Molecular Structures on Nanostructural Morphologies. *Chem. Commun.* **2007**, 1623−1625.
(7) Gao, Y.; Zhang, X.; Ma, C.; Li, X.; Jiang, J. Morphology-Controlled Self-Assembled Nanostructures of 5,15-Di[4-(5-acetylsulfanylpentyloxy)phenyl]porphyrin Derivatives. Effect of Metal−Ligand Coordination Bonding on Tuning the Intermolecular Interaction. *J. Am. Chem. Soc.* **2008**, *130*, 17044−17052.
(8) Zhang, X. J.; Zhang, X. H.; Zou, K.; Lee, C. S.; Lee, S. T. Single-Crystal Nanoribbons, Nanotubes, and Nanowires from Intramolecular Charge-Transfer Organic Molecules. *J. Am. Chem. Soc.* **2007**, *129*, 3527−3532.
(9) An, B. K.; Kwon, S. K.; Jung, S. D.; Park, S. Y. Enhanced Emission and Its Switching in Fluorescent Organic Nanoparticles. *J. Am. Chem. Soc.* **2002**, *124*, 14410−14415.
(10) Yu, H.; Qi, L. Polymer-Assisted Crystallization and Optical Properties of Uniform Microrods of Organic Dye Sudan II. *Langmuir* **2009**, *25*, 6781−6786.
(11) Ujiiye-Ishii, K.; Kwon, E.; Kasai, H.; Nakanishi, H.; Oikawa, H. Methodological Features of the Emulsion and Reprecipitation Methods for Organic Nanocrystal Fabrication. *Cryst. Growth Des.* **2008**, *8*, 369−371.
(12) Wang, Z.; Mohwald, H.; Gao, C. Nanotubes Protruding from Poly(allylamine hydrochloride)-*graft*-Pyrene Microcapsules. *ACS Nano* **2011**, *5*, 3930−3936.
(13) Zhao, Y. S.; Yang, W.; Zhang, G.; Ma, Y.; Yao, J. A Hierarchical Self-Assembly of 4,5-Diphenylimidazole on Copper. *Colloids Surf., A* **2006**, *277*, 111−118.
(14) Zhao, Y. S.; Yang, W.; Xiao, D.; Sheng, X.; Yang, X.; Shuai, Z.; Luo, Y.; Yao, J. Single Crystalline Submicrotubes from Small Organic Molecules. *Chem. Mater.* **2005**, *17*, 6430−6435.
(15) Al-Kaysi, R. O.; Müller, A. M.; Ahn, T. S.; Lee, S.; Bardeen, C. J. Effects of Sonication on the Size and Crystallinity of Stable Zwitterionic Organic Nanoparticles Formed by Reprecipitation in Water. *Langmuir* **2005**, *21*, 7990−7994.
(16) Jiang, H.; Sun, X.; Huang, M.; Wang, Y.; Li, D.; Dong, S. Rapid Self-Assembly of Oligo(*o*-phenylenediamine) into One-Dimensional Structures through a Facile Reprecipitation Route. *Langmuir* **2006**, *22*, 3358−3361.
(17) Kastler, M.; Pisula, W.; Wasserfallen, D.; Pakula, T.; Müllen, K. Influence of Alkyl Substituents on the Solution- and Surface-Organization of Hexa-*peri*-hexabenzocoronenes. *J. Am. Chem. Soc.* **2005**, *127*, 4286−4296.
(18) Zhao, Y. S.; Di, C.; Yang, W.; Yu, G.; Liu, Y.; Yao, J. Photoluminescence and Electroluminescence from Tris(8-hydroxyquinoline)aluminum Nanowires Prepared by Adsorbent-Assisted Physical Vapor Deposition. *Adv. Funct. Mater.* **2006**, *16*, 1985−1991.
(19) Fu, H.; Xiao, D.; Yao, J.; Yang, G. Nanofibers of 1,3-Diphenyl-2-pyrazoline Induced by Cetyltrimethylammonium Bromide Micelles. *Angew. Chem., Int. Ed.* **2003**, *42*, 2883−2886.
(20) Lee, J. K.; Koh, W. K.; Chae, W. S.; Kim, Y. R. Novel Synthesis of Organic Nanowires and Their Optical Properties. *Chem. Commun.* **2002**, 138−139.
(21) Jiang, L.; Fu, Y.; Li, H.; Hu, W. Single-Crystalline, Size, and Orientation Controllable Nanowires and Ultralong Microwires of Organic Semiconductor with Strong Photoswitching Property. *J. Am. Chem. Soc.* **2008**, *130*, 3937−3941.
(22) Keuren, E. V.; Georgieva, E.; Adrian, J. Kinetics of the Formation of Organic Molecular Nanocrystals. *Nano Lett.* **2001**, *1*, 141−144.
(23) Kasai, H.; Nalwa, H. S.; Oikawa, H.; Okada, S.; Matsuda, H.; Minami, N.; Kakuta, A.; Ono, K.; Mukoh, A.; Nakanishi, H. Preparation of Thin Single Crystals of Diacetylene by Pseudo-Homo Epitaxy. *Jpn. J. Appl. Phys.* **1992**, *31*, L1132−L1134.
(24) Zhang, X.; Shi, W.; Meng, X.; Lee, C.; Lee, S. Morphology-Controllable Synthesis of Pyrene Nanostructures and Its Morphology Dependence of Optical Properties. *J. Phys. Chem. B* **2005**, *109*, 18777−18780.
(25) Lee, S. J.; Hupp, J. T.; Nguyen, S. T. Growth of Narrowly Dispersed Porphyrin Nanowires and Their Hierarchical Assembly into Macroscopic Columns. *J. Am. Chem. Soc.* **2008**, *130*, 9632−9633.
(26) Hench, L. L.; Polak, J. M. Third-Generation Biomedical Materials. *Science* **2002**, *295*, 1014.
(27) Webster, T. J.; Ergun, C.; Doremus, R. H.; Siegel, R. W.; Bizios, R. Enhanced Functions of Osteoblasts on Nanophase Ceramics. *Biomaterials* **2000**, *21*, 1803.
(28) Chen, X.; Tian, X.; Shin, I.; Yoon, J. Fluorescent and Luminescent Probes for Detection of Reactive Oxygen and Nitrogen Species. *Chem. Soc. Rev.* **2011**, *40*, 4783−4804.
(29) Formica, M.; Fusi, V.; Giorgi, L.; Micheloni, M. New Fluorescent Chemosensors for Metal Ions in Solution. *Coord. Chem. Rev.* **2012**, *256*, 170−192.
(30) Cho, D. G.; Sessler, J. L. Modern Reaction-Based Indicator Systems. *Chem. Soc. Rev.* **2009**, *38*, 1647−1662.
(31) Tsukanov, A. V.; Dubanosov, A. D.; Bren, V. A.; Minkin, V. I. Organic Chemosensors with Crown-Ether Groups. *Chem. Heterocycl. Compd.* **2008**, *44*, 899−923.
(32) Callan, J. F.; de Silva, A. P.; Magri, D. C. Luminescent Sensors and Switches in the Early 21st Century. *Tetrahedron* **2005**, *61*, 8551−8588.
(33) Bell, T. W.; Hext, N. M. Supramolecular Optical Chemosensors for Organic Analytes. *Chem. Soc. Rev.* **2004**, *33*, 589−598.
(34) Rurack, K.; Resch-Genger, U. Rigidization, Preorientation and Electronic Decoupling—The "Magic Triangle" for the Design of Highly Efficient Fluorescent Sensors and Switches. *Chem. Soc. Rev.* **2002**, *31*, 116−127.
(35) Kim, H. N.; Ren, W. X.; Kim, J. S.; Yoon, J. Fluorescent and Colorimetric Sensors for Detection of Lead, Cadmium, and Mercury Ions. *Chem. Soc. Rev.* **2012**, *41*, 3210−3244.
(36) DiNatale, F.; Lancia, A.; Molino, A.; DiNatale, M.; Karatza, D.; Musmarra, D. Capture of Mercury Ions by Natural and Industrial Materials. *J. Hazard. Mater.* **2006**, *132*, 220−225.
(37) Suresh, M.; Ghosh, A.; Das, A. A Simple Chemosensor for Hg^{2+} and Cu^{2+} That Works as a Molecular Keypad Lock. *Chem. Commun.* **2008**, 3906−3908.
(38) Gao, Y.; De Galan, S.; DeBrauwere, A.; Baeyens, W.; Leermakers, M. Mercury Speciation in Hair by Headspace Injection−Gas Chromatography−Atomic Fluorescence Spectrometry (Methylmercury) and Combustion−Atomic Absorption Spectrometry (Total Hg). *Talanta* **2010**, *82*, 1919−1923.
(39) Moreno, F.; Garcia-Barrera, T.; Gomez-Ariza, J. L. Simultaneous Analysis of Mercury and Selenium Species Including Chiral Forms of Selenomethionine in Human Urine and Serum by HPLC Column-Switching Coupled to ICP-MS. *Analyst* **2010**, *135*, 2700−2705.
(40) Chai, X.; Chang, X.; Hu, Z.; He, Q.; Tu, Z.; Li, Z. Solid Phase Extraction of Trace Hg(II) on Silica Gel Modified with 2-(2-Oxoethyl)hydrazine Carbothioamide and Determination by ICP-AES. *Talanta* **2010**, *82*, 1791−1796.
(41) Fu, X.; Chen, X.; Guo, Z.; Xie, C.; Kong, L.; Liu, J.; Huang, X. Stripping Voltammetric Detection of Mercury(II) Based on a Surface Ion Imprinting Strategy in Electropolymerized Microporous Poly(2-mercaptobenzothiazole) Films Modified Glassy Carbon Electrode. *Anal. Chim. Acta* **2011**, *685*, 21−28.
(42) Bozdemir, O. A.; Guliyev, R.; Buyukcakir, O.; Selcuk, S.; Kolemen, S.; Gulseren, G.; Nalbantoglu, T.; Boyaci, H.; Akkaya, E. U. Selective Manipulation of ICT and PET Processes in Styryl−Bodipy Derivatives: Applications in Molecular Logic and Fluorescence Sensing of Metal Ions. *J. Am. Chem. Soc.* **2010**, *132*, 8029−8036.
(43) Thakur, A.; Sardar, S.; Ghosh, S. A Highly Selective Redox, Chromogenic, and Fluorescent Chemosensor for Hg^{2+} in Aqueous

DOI: 10.1021/acsami.5b01554
ACS Appl. Mater. Interfaces 2015, 7, 7476−7485

Solution Based on Ferrocene−Glycine Bioconjugates. *Inorg. Chem.* **2011**, *50*, 7066−7073.
(44) Zhang, J. F.; Kim, J. S. Small-Molecule Fluorescent Chemosensors for Hg^{2+} Ion. *Anal. Sci.* **2009**, *25*, 1271−1281.
(45) Kim, H. M.; Cho, B. R. Two-Photon Probes for Intracellular Free Metal Ions, Acidic Vesicles, and Lipid Rafts in Live Tissues. *Acc. Chem. Res.* **2009**, *42*, 863−872.
(46) Lakowicz, J. R. Principles of Fluorescence Spectroscopy, 3rd ed.; Springer: New York, 2006; p 67.
(47) Haugland, R. P. *The Handbook: A Guide to Fuorescent Probes and Labeling Technologies*, 10th ed.; Invitrogen Corp.: Carlsbad, CA, 2005.
(48) Lee, H. Y.; Swamy, K. M. K.; Jung, J. Y.; Kim, G.; Yoon, J. Rhodamine Hydrazone Derivatives Based Selective Fluorescent and Colorimetric Chemodosimeters for Hg^{2+} and Selective Colorimetric Chemosensor for Cu^{2+}. *Sens. Actuators, B* **2013**, *182*, 530−537.
(49) Wang, F.; Nam, S. W.; Guo, Z.; Park, S.; Yoon, J. A New Rhodamine Derivative Bearing Benzothiazole and Thiocarbonyl Moieties as a Highly Selective Fluorescent and Colorimetric Chemodosimeter for Hg^{2+}. *Sens. Actuators, B* **2012**, *161*, 948−953.
(50) Chen, X.; Pradhan, T.; Wang, F.; Kim, J. S.; Yoon, J. Fluorescent Chemosensors Based on Spiroring-Opening of Xanthenes and Related Derivatives. *Chem. Rev.* **2012**, *112*, 1910−1956.
(51) Bera, K.; Das, A. K.; Nag, M.; Basak, S. Development of a Rhodamine−Rhodanine-Based Fluorescent Mercury Sensor and Its Use To Monitor Real-Time Uptake and Distribution of Inorganic Mercury in Live Zebrafish Larvae. *Anal. Chem.* **2014**, *86*, 2740−2746.
(52) Lee, J. S.; Han, M. S.; Mirkin, C. A. Colorimetric Detection of Mercuric Ion (Hg^{2+}) in Aqueous Media Using DNA-Functionalized Gold Nanoparticles. *Angew. Chem., Int. Ed.* **2007**, *46*, 4093−4096.
(53) Li, D.; Wieckowska, A.; Willner, I. Optical Analysis of Hg^{2+} Ions by Oligonucleotide−Gold-Nanoparticle Hybrids and DNA-Based Machines. *Angew. Chem., Int. Ed.* **2008**, *47*, 3927−3931.
(54) Du, J.; Sun, Y.; Jiang, L.; Cao, X.; Qi, D.; Yin, S.; Ma, J.; Boey, F. Y. C.; Chen, X. Flexible Colorimetric Detection of Mercuric Ion by Simply Mixing Nanoparticles and Oligopeptides. *Small* **2011**, *7*, 1407−1411.
(55) Du, J.; Zhu, B.; Chen, X. Urine for Plasmonic Nanoparticle-Based Colorimetric Detection of Mercury Ion. *Small* **2013**, *9*, 4104−4111.
(56) Du, J.; Yin, S.; Jiang, L.; Ma, B.; Chen, X. A Colorimetric Logic Gate Based on Free Gold Nanoparticles and the Coordination Strategy between Melamine and Mercury Ions. *Chem. Commun.* **2013**, *49*, 4196−4198.
(57) Dujols, V.; Ford, F.; Czarnik, A. W. A Long-Wavelength Fluorescent Chemodosimeter Selective for Cu(II) Ion in Water. *J. Am. Chem. Soc.* **1997**, *119*, 7386−7387.
(58) Mistri, T.; Alam, R.; Dolai, M.; Mandal, S. K.; Guha, P.; KhudaBukhsh, A. R.; Ali, M. Rhodamine-Based Chromo-/Fluorogenic Dual Signalling Probe for Selective Recognition of Hg(II) with Potential Applications for INHIBIT Logic Devices and Cell-Imaging Studies. *Eur. J. Inorg. Chem.* **2013**, 5854−5861.
(59) Zahran, M. A. H.; Abdin, Y. G.; Osman, A. M. A.; Gamal-Eldeen, A. M.; Talaat, R. M.; Pedersen, E. B. Synthesis and Evaluation of Thalidomide and Phthalimide Esters as Antitumor Agents. *Arch. Pharm. Chem. Life Sci.* **2014**, *347*, 642−649.
(60) Huang, L.; Wang, X.; Xie, G.; Xi, P.; Li, Z.; Xu, M.; Wu, Y.; Baib, D. A New Rhodamine-Based Chemosensor for Cu^{2+} and the Study of Its Behaviour in Living Cells. *Dalton Trans.* **2010**, *39*, 7894−7896.
(61) Lohani, C. R.; Kim, J. M.; Chung, S. Y.; Yoon, J.; Lee, K. H. Colorimetric and Fluorescent Sensing of Pyrophosphate in 100% Aqueous Solution by a System Comprised of Rhodamine B Compound and Al^{3+} Complex. *Analyst* **2010**, *135*, 2079.
(62) Alam, R.; Mistri, T.; Mondal, P.; Das, D.; Mandal, S. K.; Khuda-Bukhsh, A. R.; Ali, M. A Novel Copper(II) Complex as a Nitric Oxide Turn-On Fluorosensor: Intracellular Applications and DFT Calculation. *Dalton Trans.* **2014**, *43*, 2566−2576.
(63) Alam, R.; Mistri, T.; Katarkar, A.; Chaudhuri, K.; Mandal, S. K.; Khuda-Bukhsh, A. R.; Das, K. K.; Ali, M. A Novel Chromo- and Fluorogenic Dual Sensor for Mg^{2+} and Zn^{2+} with Cell Imaging Possibilities and DFT studies. *Analyst* **2014**, *139*, 4022−4030.
(64) Bhowmick, R.; Dolai, M.; Alam, R.; Mistri, T.; Katarkar, A.; Chaudhuri, K.; Ali, M. A Novel Pyrene-2-(pyridin-2-ylmethylsulfanyl)-ethylamine Based Turn-On Dual Sensor for Al^{3+}: Experimental and Computational Studies. *RSC Adv.* **2014**, *4*, 41784−41792.
(65) Skoog, D. A.; West, D. M.; Holler, F. J. *Fundamentals of Analytical Chemistry*, 7th ed.; Harcourt College Publishers: San Diego, CA, 1996.
(66) Chakrabarty, A.; Mallick, A.; Haldar, B.; Das, P.; Chattopadhyay, N. Binding Interaction of a Biological Photosensitizer with Serum Albumins: A Biophysical Study. *Biomacromolecules* **2007**, *8*, 920−927.
(67) Wu, D.; Huang, W.; Lin, Z.; Duan, C.; He, C.; Wu, S.; Wang, D. Highly Sensitive Multiresponsive Chemosensor for Selective Detection of Hg^{2+} in Natural Water and Different Monitoring Environments. *Inorg. Chem.* **2008**, *47*, 7190−7201.
(68) Mahato, P.; Saha, S.; Suresh, E.; Liddo, R. D.; Parnigotto, P. P.; Conconi, M. T.; Kesharwani, M. K.; Ganguly, B.; Das, A. Ratiometric Detection of Cr^{3+} and Hg^{2+} by a Naphthalimide−Rhodamine Based Fluorescent Probe. *Inorg. Chem.* **2012**, *51*, 1769−1777.
(69) Wang, H.; Li, Y.; Xu, S.; Li, Y.; Zhou, C.; Fei, X.; Sun, L.; Zhang, C.; Li, Y.; Yang, Q.; Xu, X. Rhodamine-Based Highly Sensitive Colorimetric Off−On Fluorescent Chemosensor for Hg^{2+} in Aqueous Solution and for Live Cell Imaging. *Org. Biomol. Chem.* **2011**, *9*, 2850−2855.
(70) Wang, Y.; Huang, Y.; Li, B.; Zhang, L.; Song, H.; Jiang, H.; Gao, J. A Cell Compatible Fluorescent Chemosensor for Hg^{2+} Based on a Novel Rhodamine Derivative That Works as a Molecular Keypad Lock. *RSC Adv.* **2011**, *1*, 1294−1300.

DOI: 10.1021/acsami.5b01554
ACS Appl. Mater. Interfaces 2015, 7, 7476−7485